ARTICLE OPEN

Check for updates

# Autonomous quantum error correction and fault-tolerant quantum computation with squeezed cat qubits

Qian Xu[1,4], Guo Zheng[1,4], Yu-Xin Wang[1], Peter Zoller[2,3], Aashish A. Clerk[1] and Liang Jiang[1]✉

We propose an autonomous quantum error correction scheme using squeezed cat (SC) code against excitation loss in continuous-variable systems. Through reservoir engineering, we show that a structured dissipation can stabilize a two-component SC while autonomously correcting the errors. The implementation of such dissipation only requires low-order nonlinear couplings among three bosonic modes or between a bosonic mode and a qutrit. While our proposed scheme is device independent, it is readily implementable with current experimental platforms such as superconducting circuits and trapped-ion systems. Compared to the stabilized cat, the stabilized SC has a much lower dominant error rate and a significantly enhanced noise bias. Furthermore, the bias-preserving operations for the SC have much lower error rates. In combination, the stabilized SC leads to substantially better logical performance when concatenating with an outer discrete-variable code. The surface-SC scheme achieves more than one order of magnitude increase in the threshold ratio between the loss rate $\kappa_1$ and the engineered dissipation rate $\kappa_2$. Under a practical noise ratio $\kappa_1/\kappa_2 = 10^{-3}$, the repetition-SC scheme can reach a $10^{-15}$ logical error rate even with a small mean excitation number of 4, which already suffices for practically useful quantum algorithms.

*npj Quantum Information* (2023)9:78 ; https://doi.org/10.1038/s41534-023-00746-0

## INTRODUCTION

Quantum information is fragile to errors introduced by the environment. Quantum error correction (QEC) protects quantum systems by correcting the errors and removing the entropy[1–3]. Based upon QEC, fault-tolerant quantum computation (FTQC) can be performed, provided that the physical noise strength is below an accuracy threshold[4–7]. However, realizing FTQC is yet challenging due to the demanding threshold requirement and the significant resource overhead[8–11]. Unlike discrete-variable (DV) systems, continuous-variable (CV) systems possess an infinite-dimensional Hilbert space. Encoding the quantum information in CV systems, therefore, provides a hardware-efficient approach to QEC[12–16]. Various bosonic codes have been experimentally demonstrated to suppress errors in CV systems[17–22].

The standard QEC procedure relies on actively measuring the error syndromes and performing feedback controls[1]. However, such adaptive protocols demand fast, high-fidelity coherent operations and measurements, which poses significant experimental challenges. At this stage, the error rates in the encoded level are still higher than the physical error rates in current devices due to the errors during the QEC operations[23–26]. To address these challenges, we may implement QEC non-adaptively via engineered dissipation - an approach called autonomous QEC (AutoQEC)[27,28]. Such an approach avoids the measurement imperfection and overhead associated with the classical feedback loops. AutoQEC schemes that can greatly suppress dephasing noise in bosonic systems have been both theoretically investigated and experimentally demonstrated using the two-component cat code[20,22,29–33]. However, AutoQEC against excitation loss, which is usually the dominant error source in a bosonic mode, remains challenging. It requires either large nonlinearities that are challenging to engineer (e.g., the multiphoton processes needed for $n$-fold rotation-symmetrical codes with $n \geq 4$[29,34,35]) or couplings to an intrinsically nonlinear DV system[19,36,37] that is much noisier than the bosonic mode.

In this work, we propose an AutoQEC scheme against excitation loss with low-order nonlinearities and accessible experimental resources. Our scheme is, in principle, device-independent and readily implementable in superconducting circuits and trapped-ion systems. The scheme is based on the squeezed cat (SC) encoding[38], which involves the superposition of squeezed coherent state. We introduce an explicit AutoQEC scheme for the SC against loss errors by engineering a nontrivial dissipation, which simultaneously stabilizes the SC states and corrects the loss errors. We show that the engineered dissipation is close to the optimal recovery obtained using a semidefinite programming[39–41]. Notably, our proposed dissipation can be implemented with the same order of nonlinearity as that required by the two-component cat, which has been experimentally demonstrated in superconducting circuits[20,42,43] and shown to be feasible in trapped-ion systems[44].

Furthermore, we show that similar to the stabilized cat qubits, the stabilized SC qubits also possess a biased noise channel (with one type of error dominant over others), with an even larger bias (defined to be the ratio between the dominant error rate and the others) $\sim e^{\bar{n}^2}$ (compared to $\sim e^{\bar{n}}$ for the cat), where $\bar{n}$ denotes the mean excitation number of the codewords. Consequently, we can concatenate the stabilized SC qubits with a DV code tailored towards the biased noise to realize low-overhead fault tolerant QEC and quantum computation[45–50]. We develop a set of operations for the SC that are compatible with the engineered dissipation and can preserve the noise bias needed for the concatenation. Compared to those for the cat[30], these operations suffer less from the loss errors because of the AutoQEC. Moreover, they can be implemented faster due to a larger effective dissipation gap and a cancellation of the leading-order non-

[1]Pritzker School of Molecular Engineering, The University of Chicago, Chicago 60637 IL, USA. [2]Institute for Theoretical Physics, University of Innsbruck, Innsbruck A-6020, Austria. [3]Institute for Quantum Optics and Quantum Information of the Austrian Academy of Sciences, Innsbruck A-6020, Austria. [4]These authors contributed equally: Qian Xu, Guo Zheng. ✉email: liang.jiang@uchicago.edu

adiabatic errors. In combination, the access to higher-quality operations leads to much better logical performance in the concatenated level using the SC qubits. For instance, we can achieve one-to-two orders of magnitude improvement in the $\kappa_1/\kappa_2$ threshold, where $\kappa_1$ is the excitation loss rate and $\kappa_2$ is the engineered dissipation rate, for the surface-SC and repetition-SC scheme (compared to surface-cat and repetition-cat, respectively). Furthermore, the repetition-SC can achieve a logical error rate as low as $10^{-15}$, which already suffices for many useful quantum algorithms[8,51], even using a small SC with $\bar{n} = 4$ under a practical noise ratio $\kappa_1/\kappa_2 = 10^{-3}$.

We note that aspects of the SC encoding were also recently studied in ref. [38], with an emphasis on the enhanced protection against dephasing provided by squeezing (a point already noted in refs. [52–54]). Unlike our work, ref. [38] neither explored the enhanced noise bias provided by squeezing, nor exploited the ability to concatenate the SC code with outer DV codes using bias-preserving operations; as we have discussed, these are key advantages of the SC approach. Our work also goes beyond ref. [38] in providing an explicit, fully autonomous approach to SC QEC that exploits low-order nonlinearities, and it is compatible with several experimental platforms. In contrast, ref. [38] studied an approach requiring explicit syndrome measurements and a formal, numerically-optimized recovery operation. It was unclear how such an operation could be feasibly implemented in experiment. We also note that the SC has also been studied in the context of quantum transduction[55] (a very different setting than that considered here) and preparation of SC states has been recently demonstrated experimentally[56].

## RESULTS

### Squeezed cat encoding

The codewords of the SC are defined by applying a squeezing along the displacement axis (which is taken to be real) to the cat codewords:

$$\left|\mathrm{SC}^{\pm}_{r,\alpha'}\right\rangle := \hat{S}(r)\left|C^{\pm}_{\alpha'}\right\rangle \tag{1}$$

where $\left|C^{\pm}_{\alpha'}\right\rangle := \mathcal{N}_{\pm}(|\alpha'\rangle + |-\alpha'\rangle)$ with $\mathcal{N}_{\pm} = \frac{1}{\sqrt{2(1\pm e^{-2\alpha'^2})}}$ being normalization factors, and $\hat{S}(r) := \exp[\frac{r}{2}(\hat{a}^2 - \hat{a}^{\dagger 2})]$ is the squeezing operator. The above codewords with even ($|\mathrm{SC}^{+}_{r,\alpha'}\rangle$) and odd ($|\mathrm{SC}^{-}_{r,\alpha'}\rangle$) excitation number parity are defined to be the X-basis eigenstates. Similar to other bosonic codes[16], the performance of the SC code is related to the mean excitation number $\bar{n}$ of the codewords:

$$\begin{aligned}\bar{n} &:= \tfrac{1}{2}\left(\langle \mathrm{SC}^{+}_{r,\alpha'}|\hat{a}^{\dagger}\hat{a}|\mathrm{SC}^{+}_{r,\alpha'}\rangle + \langle \mathrm{SC}^{-}_{r,\alpha'}|\hat{a}^{\dagger}\hat{a}|\mathrm{SC}^{-}_{r,\alpha'}\rangle\right)\\ &= \alpha'^2(\coth 2\alpha'^2 \cosh 2r - \sinh 2r) + \sinh^2 r\end{aligned} \tag{2}$$

For a SC code with fixed $\bar{n}$, according to Eq. (2), the amplitude $\alpha'$ of the underlying coherent states varies with the squeezing parameter $r$ as

$$\alpha' \approx \sqrt{\bar{n} - \sinh^2 r}e^{r}, \tag{3}$$

which holds for the regime of interest where $\alpha'>1$. See a graphic illustration of the interdependency between $\bar{n}, \alpha'$ and $r$ in Supplementary Note 2. Note that $\alpha'$ is closely related to how separated in phase space the two computational-basis states are, which determines their resilience against local error processes[16,29]. At fixed $\bar{n}$, $\alpha'^2$ can be written as a concave quadratic function of $e^{2r}$, which has a maximum $\alpha'^2_{\max} = \bar{n}^2 + \bar{n}$ (see Supplementary Note 2).

For the SC, it is convenient to consider the subsystem decomposition of the oscillator Hilbert space $\mathcal{H} = \mathcal{H}_L \otimes \mathcal{H}_g$, where $\mathcal{H}_L$ represents a logical sector of dimension 2 (which we refer to as a logical qubit) and $\mathcal{H}_g$ represents a gauge sector of infinite dimension (which we refer to as a gauge mode). Analogous to the modular subsystem decomposition of the GKP qubit[57], whose logical sector carries the modular value of the quadratures, the logical sector of the SC carries the parity information (excitation number modulo 2). Similar decomposition for the cat was used in refs. [32,58]. We can choose a basis under the subsystem decomposition spanned by squeezed displaced Fock states $|\pm\rangle_L \otimes |\hat{\bar{n}} = n\rangle_g \approx \mathcal{N}_{\pm,n}\hat{S}(r)[\hat{D}(\alpha') \pm (-1)^n\hat{D}(-\alpha')]|n\rangle$ (we use $\approx$ since the right-hand side should be orthonormalized within each parity branch. See Supplementary Note 1 for details). By choosing this basis, the SC codewords in Eq. (1) coincide with $|\pm\rangle_L \otimes |\hat{\bar{n}} = 0\rangle_g$, i.e., the codespace is the two-dimensional subspace obtained by projecting the gauge mode to the ground state. Furthermore, the bosonic annihilation operator $\hat{a}$ can be expressed as

$$\hat{a} = \hat{Z}_L \otimes (e^{-r}\alpha' + \cosh r\hat{\bar{a}} - \sinh r\hat{\bar{a}}^{\dagger}) + \mathcal{O}(e^{-2\alpha'^2}), \tag{4}$$

where $\hat{Z}_L$ is the Pauli Z operator acting on the logical qubit, and $\hat{\bar{a}} = \sum_{n=0}^{\infty}\sqrt{n+1}|\hat{\bar{n}} = n\rangle_g\langle\hat{\bar{n}} = n+1|$ is the annihilation operator acting on the gauge mode.

Typical bosonic systems suffer from excitation loss ($\hat{a}$), heating ($\hat{a}^{\dagger}$), and dephasing ($\hat{a}^{\dagger}\hat{a}$) errors, with loss being the prominent one[16]. We now explain why the SC code can correct the loss errors by analyzing the Knill-Laflamme error correction conditions[59,60] and evaluating the QEC matrices[16]. Consider a pure loss channel with a loss probability $\gamma$, the leading-order Kraus operators are $\{\hat{I}, \sqrt{\gamma}\hat{a}\}$. The detectability of a single excitation loss is quantified by the matrix:

$$\begin{aligned}\hat{P}_{\mathrm{code}}\hat{a}\hat{P}_{\mathrm{code}} &= e^{-r}\alpha'\tfrac{q+q^{-1}}{2}\hat{Z}_c + ie^{r}\alpha'\tfrac{q-q^{-1}}{2}\hat{Y}_c\\ &\approx \sqrt{\bar{n} - \sinh^2 r}\hat{Z}_c - ie^{r}\alpha' e^{-2\alpha'^2}\hat{Y}_c,\end{aligned} \tag{5}$$

where $\hat{P}_{\mathrm{code}}$ is the projection onto the code space, $\hat{Z}_c := \hat{Z}_L \otimes |0\rangle_g\langle 0|$ ($\hat{Y}_c := \hat{Y}_L \otimes |0\rangle_g\langle 0|$) is the Pauli $Z$ ($Y$) operator in the code space, and $q := \sqrt{\frac{1-e^{-2\alpha'^2}}{1+e^{-2\alpha'^2}}}$. See Supplementary Note 2 for a detailed derivation. The approximation in the second line is made in the regime of interest where $e^{-2\alpha'^2} \ll 1$.

Eq. (5) indicates that a single excitation loss mostly leads to an undetectable logical phase-flip error with a probability that decrease with the squeezing parameter $r$, which can be better understood by considering the action of the decomposed $\hat{a}$ operator (Eq. (4)) on the codeword $\hat{a}(|+\rangle_L \otimes |0\rangle_g) = |-\rangle_L \otimes\sqrt{\bar{n}}(\sqrt{\eta}|0\rangle_g - \sqrt{1-\eta}|1\rangle_g)$, where

$$\eta := (\bar{n} - \sinh^2 r)/\bar{n}. \tag{6}$$

As shown in Fig. 1, after a single excitation loss, the branch of the population (with ratio $\eta$) that stays in the ground state of the gauge mode leads to undetectable logical phase-flip errors. In contrast, the other branch (with ratio $1-\eta$) that goes to the first excited gauge state is in principle detectable. The detectable branch is also approximately correctable since $\hat{P}_{\mathrm{code}}\hat{a}^{\dagger}\hat{a}\hat{P}_{\mathrm{code}} \approx \bar{n}\hat{I}_c + \mathcal{O}(e^{-2\alpha'^2})\hat{X}_c$. Therefore, we expect that we can suppress the loss-induced phase flip errors by a factor $\eta$ that decreases with the squeezing $r$. Moreover, the $\hat{X}_c$ and $\hat{Y}_c$ terms in the QEC matrices for both loss, heating, and dephasing are exponentially suppressed by $\alpha'^2$. As shown in Eq. (3), $\alpha'^2$ can be greatly increased by adding squeezing (with $\alpha'^2_{\max} = \bar{n}^2 + \bar{n}$). Consequently, we expect that the SC can also have significantly enhanced noise bias compared to the cat.

### Autonomous quantum error correction

While we have shown that the SC encoding can, in principle, detect and correct the loss errors, it remains a non-trivial task to find an explicit and practical recovery channel. In this section, we

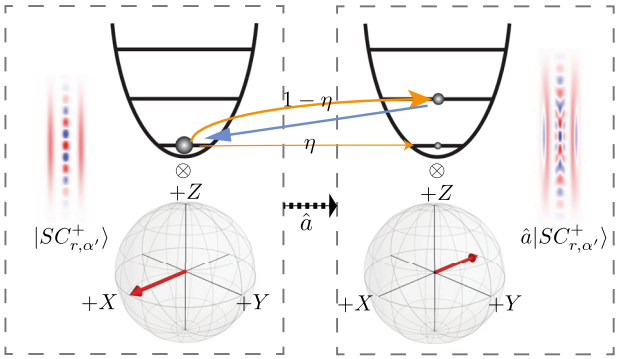


**Fig. 1 The illustration of a SC that suffers from a single excitation loss and then approximately corrects it.** Each dashed box represents a state (visualized by the Wigner function) of the SC, which is decomposed as a product of a logical qubit and a gauge mode. A single excitation loss corrupts the codeword $|+\rangle_c$ (left) into the state $\hat{a}|+\rangle_c/\sqrt{\langle+|_c\hat{a}^\dagger\hat{a}|+\rangle_c}$ (right). During such a process, a phase flip happens on the logical qubit, and a fraction $1-\eta$ of the gauge mode population gets excited (indicated by the thick orange arrow). The excited population can be detected and then corrected, as indicated by the blue arrow.

provide such a recovery channel, showing surprisingly that it requires only experimental resources that have been previously demonstrated.

As shown by the blue arrow in Fig. 1, we can, in principle, perform photon counting measurement on a probe field that is weakly coupled to the gauge mode, and apply a feedback parity flip $\hat{Z}_L$ on the logical qubit upon detecting an excitation in the probe field[61]. Such measurement and feedback process can be equivalently implemented by applying the dissipative dynamics as described by Lindblad master equation $\frac{d\hat{\rho}}{dt}=\kappa_2\mathcal{D}[\hat{F}]$, with the jump operator $\hat{F}$ given by

$$\hat{F}=(\hat{Z}_L\otimes\hat{\mathbb{I}})\hat{S}(r)(\hat{a}^2-\alpha'^2)\hat{S}^\dagger(r), \tag{7}$$

and $\mathcal{D}[\hat{A}]\hat{\rho}:=\hat{A}\hat{\rho}\hat{A}^\dagger-\frac{1}{2}\{\hat{A}^\dagger\hat{A},\hat{\rho}\}$. When $\alpha'\gg1$, $\hat{F}\propto\hat{Z}_L\otimes\hat{a}$ represents a logical phase flip conditioned on the gauge mode losing an excitation. In the Fock basis, such an operator can be approximately given by

$$\hat{F}\approx\frac{1}{\alpha'}\hat{S}(r)(c_1\hat{a}+c_2\hat{a}^\dagger)(\hat{a}^2-\alpha'^2)\hat{S}^\dagger(r), \tag{8}$$

with $c_1+c_2=1$ (see Supplementary Note 1 for more details).

In Methods, we propose two reservoir-engineering approaches to implement such a nontrivial dissipator using currently accessible experimental resources. We sketch the main ideas here. The first approach utilizes three bosonic modes that are nonlinearly coupled. As shown in Fig. 5a, a high-quality mode $b$ and a lossy mode $c$, together, serve as a nonreciprocal bath[62] that provides a directional interaction $e^{-i\theta\hat{Z}_L}\otimes\hat{a}$ from the gauge mode to the logical qubit in the storage mode $a$. Such a coupled system can be physically realized in, e.g., superconducting circuits[42,43]. The second approach couples a bosonic mode nonlinearly to a qutrit $\{|g\rangle,|e\rangle,|f\rangle\}$. As shown in Fig. 6, the bosonic mode is coupled to the $gf$ transition via $\hat{S}(r)(\hat{a}^2-\alpha'^2)\hat{S}^\dagger(r)|f\rangle\langle g|+h.c.$ and to the $ef$ transition via $\hat{Z}_L|e\rangle\langle f|+h.c.$. By enhacing the decay from $|e\rangle$ to $|g\rangle$, we can obtain the effective dissipator $\hat{F}$ by adiabatically eliminating both $|e\rangle$ and $|f\rangle$. Such a system can be physically realized in, e.g., trapped-ion system[44].

With the engineered dissipator in Eq. (7), the SC can be autonomously protected from excitation loss, heating and dephasing. We now derive the error channel of the dissipatively stabilized SC qubit in the memory level. The dynamics of the system are described by the Lindblad master equation:

$$\begin{aligned}\frac{d\hat{\rho}}{dt}=&\kappa_2\mathcal{D}[\hat{F}]\hat{\rho}+\kappa_1(1+n_{\rm th})\mathcal{D}[\hat{a}]\hat{\rho}\\&+\kappa_1 n_{\rm th}\mathcal{D}[\hat{a}^\dagger]\hat{\rho}+\kappa_\phi\mathcal{D}[\hat{a}^\dagger\hat{a}]\hat{\rho}.\end{aligned} \tag{9}$$

The logical phase-flip and bit-flip error rates of the SC under the dynamics described by Eq. (9) can be analytically obtained (see Methods for the derivations):

$$\gamma_Z=[\kappa_1(1+2n_{\rm th})+\kappa_\phi e^{-2r}](\bar{n}-\sinh^2 r), \tag{10}$$

$$\gamma_{X,Y}=\kappa_\phi\frac{(\bar{n}-\sinh^2 r)e^{2r}(\sinh^2 2r/4+\cosh 4r)}{2\sinh\left[2(\bar{n}-\sinh^2 r)e^{2r}\right]}, \tag{11}$$

where $\gamma_{X,Y}$ denotes the sum of the logical $X$ and $Y$ error rates, which we refer to as the bit-flip rate for simplicity. Note that similar to the cat[63], the full error channel of the stabilized SC, which is analyzed in detail in Supplementary Note 3, is not a Pauli error channel in general. For simplicity, we make the Pauli-twirling approximation only keeping the diagonal terms of the process matrix in the Pauli basis. We only consider the dephasing error $\kappa_\phi\mathcal{D}[\hat{a}^\dagger\hat{a}]$ for $\gamma_{X,Y}$ since the loss-induced bit-flip rate has a more favorable scaling $\sim e^{-4\alpha'^2}$ with $\alpha'$[58,64]. The loss and the heating contribute to $\gamma_Z$ in the same way (both suppressed by a factor $\eta$) since their undetectable portion ($\eta$) is the same (see Eq. (4) and its hermitian conjugate). The dephasing also contributes to $\gamma_Z$, but with an extra $e^{-2r}$ suppression, when combined with the parity-flipping dissipator $\hat{F}$. See Methods for details. Setting $r=0$ and removing the $\kappa_\phi$ term in $\gamma_Z$, we restore the error rates of the dissipative cat[30].

In the regime where $e^{-r}\ll1$ and $\gamma_Z$ is mainly contributed by excitation loss, we can simplify Eqs. (10) and (11) as

$$\gamma_Z\approx\eta\bar{n}\kappa_1,\gamma_{X,Y}\approx\frac{9}{16}\kappa_\phi\alpha'^2e^{-2\alpha'^2}e^{4r}, \tag{12}$$

where

$$\alpha'\approx\sqrt{4\eta(1-\eta)\bar{n}}. \tag{13}$$

As plotted in Fig. 2a, fixing $\bar{n}$, $\gamma_Z$ decreases monotonically with the squeezing $r$ (unless $r$ approaches the maximum squeezing $r_{\max}\approx\sinh^{-1}(\sqrt{\bar{n}})$. See Methods for details.) as the undetectable portion $\eta$ of the loss-induced errors decreases (see Eq. (6)). The change of $\gamma_{X,Y}$ with $r$ (or equivalently, $\eta$) is roughly captured by the change in the displacement amplitude $\alpha'$ (see Eq. (13)), and $\gamma_{X,Y}$ takes the minima roughly when $\alpha'$ reaches the maxima $\alpha'_{\max}=\sqrt{\bar{n}^2+\bar{n}}$. Note that the minimal bit-flip rate of the SC enjoys a more favorable scaling $\gamma_{X,Y}\propto e^{-2\bar{n}}$ with $\bar{n}$, compared to $\gamma_{X,Y}\propto e^{-\bar{n}}$ for the cat, so that the SC can have a much larger noise bias under the same excitation number constraint.

In principle, one needs to consider the tradeoff between $\gamma_Z$ and $\alpha'$ and choose the optimal $\eta$ depending on the tasks of interest. Smaller $\eta$ leads to better protection from excitation losses, which is preferred by, e.g., the idling operations. Larger $\alpha'$, on the other hand, leads to a larger noise bias and a widened effective dissipation gap, which can support faster operations, e.g., the bias-preserving CNOT gate introduce in the next section. Here, the effective dissipation gap is defined as the the excitation gap of the effective Hamiltonian $\hat{H}_{\rm eff}=\frac{1}{2}\kappa_2\hat{F}^\dagger\hat{F}=\frac{1}{2}\kappa_2\hat{S}(r)(\hat{a}^{\dagger2}-\alpha'^2)(\hat{a}^2-\alpha'^2)\hat{S}^\dagger(r)$, which characterizes the leakage rate and the non-adiabatic error rate under a Hamilotnian perturbation[30,58,65]. Since $\hat{H}_{\rm eff}$ is the same as that for a cat with a displacement $\alpha'$ up to a unitary transformation, the effective dissipation gap for the dissipative SC is $2\kappa_2\alpha'^2$. In the following, we fix $\bar{n}=4$ and $\eta=1/4$ if not specified otherwise, which corresponds to a squeezing of $r=1.32$ (11.5 dB). Such a parameter choice leads to $\gamma_Z\approx\kappa_1$, which removes the enhancement factor $\bar{n}$ present for the stabilized cats[30,31] (for $\bar{n}=4$). Meanwhile, $\alpha'^2\approx\frac{3}{4}\bar{n}^2$

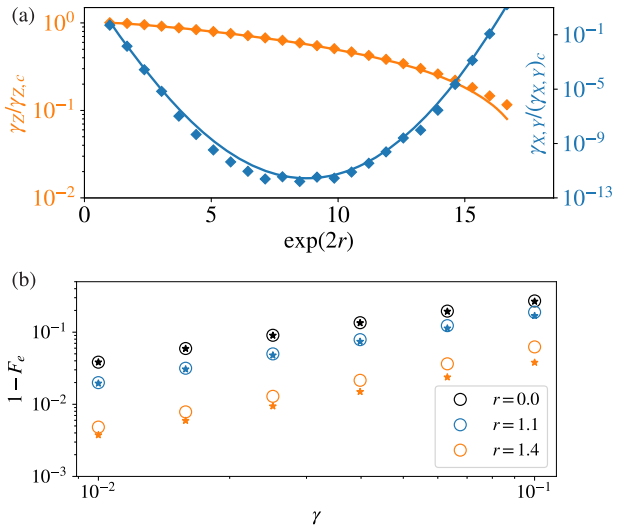


**Fig. 2 Error rates of the stabilized SC. a** The phase $\gamma_Z$ (orange) and bit $\gamma_{X,Y}$ (cyan) error rate of the dissipatively stabilized SC as a function of squeezing $r$ under the parameters $\bar{n} = 4, \kappa_1 = 100\kappa_\phi = \kappa_2/100, n_{\text{th}} = 0.01$. The solid lines represent the analytical expressions Eqs. (10) and (11) while the diamonds represent the numerically extracted values. All the error rates are normalized by those of the dissipative cat $\gamma_{Z,c}, (\gamma_{X,Y})_c$, which are given by Eqs. (10) and (11) with $r = 0$. **b** The entanglement infidelity of a joint loss and recovery channel varying with the loss probability $\gamma$ for the SC encoding with $\bar{n} = 4$. The recovery channel is either the engineered dissipation (the circles) or the optimal recovery channel determined by an SDP program[39–41] (the stars).

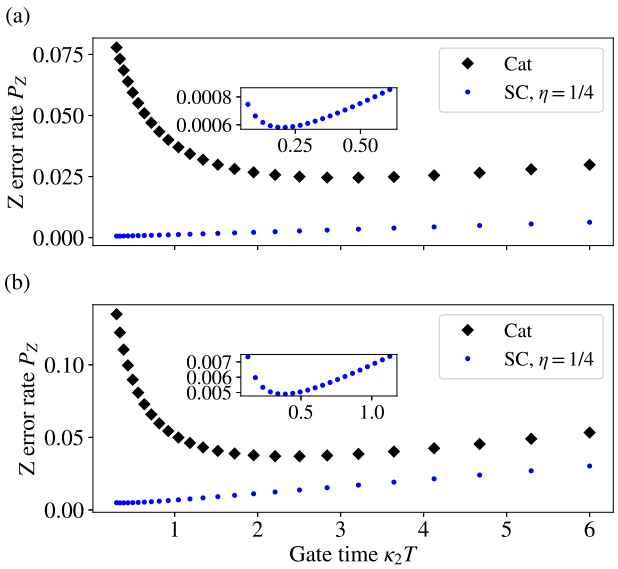


**Fig. 3 Error rates of the bias-preserving *Z*-rotation and CNOT gate for the stabilized SC.** We plot the total $Z$ error probability of the $Z(\pi)$ gates (**a**) and the CNOT gates (**b**) versus the gate time. For the CNOT gate, $p_Z := p_{Z_c} + p_{Z_t} + p_{Z_cZ_t}$ is the sum of the control-mode, target-mode, and the correlated phase flip rates. $\kappa_1/\kappa_2$ is fixed at $10^{-3}$. The blue lines represent the gates on the cat qubits[30], and the red lines represent our proposed gates on the SC qubits with $\eta = 1/4$. $\bar{n}$ is chosen as 4 for both cat and SC. The insets are the zoomed-in error rates of the SC gates around the optimal gate times. As detailed in Methods, the $Z(\pi)$ gate requires a linear drive of strength $\frac{\pi}{8T}$ ($\frac{\pi}{4T}$) for the cat (SC). The CNOT gate requires a nonlinear coupling between the control and the target mode of strength $\frac{\pi}{8T}$ ($\frac{\pi}{4T}$) for the cat (SC).

provides a sufficiently large noise bias and a large effective dissipation gap.

In Fig. 2b, we benchmark the performance of our Auto-QEC scheme against loss errors by comparing it to the optimal recovery channel given by a semidefinite programming (SDP) method[39–41]. We consider the composite channel $\mathcal{N} = \mathcal{D} \cdot \mathcal{N}_\gamma \cdot \mathcal{E}$, where $\mathcal{E}$ denotes the encoding map from a qubit to the SC, $\mathcal{N}_\gamma$ denotes a Gaussian pure loss channel (corresponding to Eq. (9) with $\kappa_2 = \kappa_\phi = n_{\text{th}} = 0$) with loss probability $\gamma := \kappa_1 t$, and $\mathcal{D}$ denotes the recovery channel either using the autonomous QEC with the dissipator Eq. (7) or the optimal recovery channel. We use the entanglement fidelity $F_e := \langle\Phi^+|(\mathcal{N} \otimes \mathcal{I})(|\Phi^+\rangle\langle\Phi^+|)|\Phi^+\rangle$, where $|\Phi^+\rangle$ denotes a Bell state for the logical qubit and an ancilla qubit, as the error metric for the composite channel. We evaluate the entanglement infidelity (EI) $1 - F_e$ as a function of the loss probability $\gamma$. Note that the EI is the objective function for the SDP. As shown in Fig. 2b, the EI obtained using the Auto-QEC is close to the optimal EI, especially in the low-$\gamma$ regime, demonstrating that our proposed autonomous QEC scheme is close to optimal for correcting excitation loss errors. We note that it is crucial to have the phase-flip $\hat{Z}_L$ correction in the dissipator $\hat{F}$ in order to correct the loss-induced phase-flip errors. Otherwise, a simple dissipator $\hat{S}(r)(\hat{a}^2 - \alpha'^2)\hat{S}^\dagger(r)$ directly generalized from the dissipative cat would still give an unsuppressed phase-flip rate $\gamma_Z = \kappa_1\bar{n}$.

We note that the SC encoding also emerges as the optimal or close-to-optimal single-mode bosonic code through a bi-convex optimization (alternating SDP) procedure for a loss and dephasing channel with dephasing being dominant, as shown in ref. [66].

## Bias-preserving operations

To apply the autonomously protected SC for computational tasks, we need to develop a set of gate operations that are compatible with the engineered dissipation. Furthermore, the operations should preserve the biased noise channel of the SC, which can be utilized for resource-efficient concatenated QEC and fault-tolerant quantum computing[49,50,58,67,68]. Following the literature for the cat and the pair-cat[30,63,69,70], we develop a set of bias-preserving operations $\mathcal{B} = \{\mathcal{P}_{|\pm\rangle_c}, \mathcal{M}_X, X, Z(\theta), ZZ(\theta), \text{CNOT}, \text{Toffoli}\}$ for the SC, which suffice for many concatenated QEC schemes (e.g., concatenation with the repetition codes or the surface codes). The detailed design of each operation is presented in Methods.

Overall, the bias-preserving operations for the SC can achieve much higher fidelity (lower dominant $Z$-type error rates) than those for the cat for the following two reasons: (1). The operations suffer less from the excitation loss errors, which are (partially) autonomously corrected. (2). The non-adiabatic errors are significantly suppressed by the $\hat{Z}_L$ correction in the dissipator $\hat{F}$ (see Eq. (7)) and the enlarged effective dissipation gap ($\propto \alpha'^2$), so that the gate operations could be implemented faster. In Fig. 3, we show the total $Z$-type error rates for the Z-axis rotation $Z(\theta)$ and the CNOT gate as a function of the gate time. Compared to the cat gates in ref. [30] with the same $\bar{n}$, the SC $Z(\theta)$ (CNOT) gate can achieve a 42.0 (7.56) times reduction in the lowest error rates. While we have fixed $\eta = 1/4$ as mentioned in last section, it is not necessarily the optimal choice of the squeezing. In fact, with $\eta$ approaching 1/2, we obtain even lower errors at faster gate times.

We note that compared to the cat stabilized by $\hat{a}^2 - \alpha^2$ in the literature, a simple extension to a SC stabilized by $\hat{S}(r)(\hat{a}^2 - \alpha'^2)\hat{S}^\dagger(r)$ can also lead to improvement in the gate speed and fidelities due to the enlarged effective dissipation gaps. However, adding the extra phase flip in the dissipator brings a much more significant improvement due to the suppression of the loss-induced errors and the leading-order non-adiabatic errors. See Discussion for more details.

## Concatenated quantum error correction

With the bias-preserving operations, we can concatenate the SC with an outer discrete-variable code to suppress the logical error

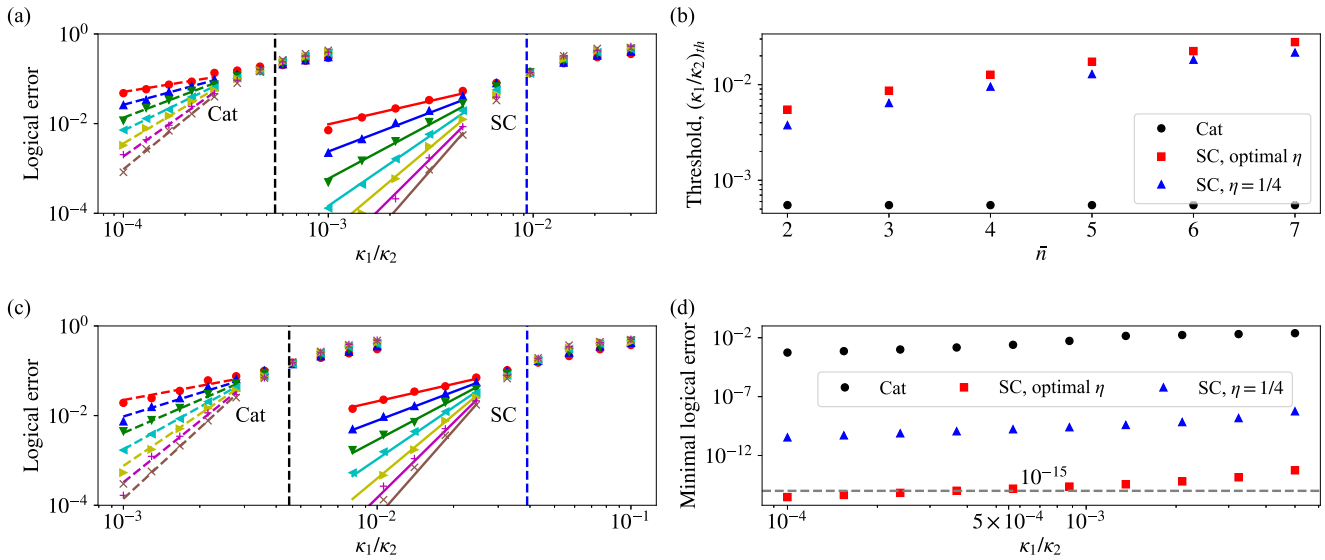


**Fig. 4 Logical errors of the SC and the cat concatenated with repetition codes or surface codes. a** Surface code logical $Z$ error probabilities for a range of code distance $d_Z = 3, 5, 7, ..., 15$ (from red to brown) with fixed $d_X = 3$. The SC is fixed to $\bar{n} = 4, \eta = 1/4$. The dashed lines indicate the threshold values of $\kappa_1/\kappa_2$. **b** Surface code thresholds in $\kappa_1/\kappa_2$ varying with the average excitation number of the SC or the cat. **c** Repetition code logical $Z$ error probabilities for a range of code size $d_Z$. **d** Repetition code minimum total logical error probabilities, under the long gate time constraint $T \geq 1/\kappa_2$. Both the cat and the SC have an average excitation number $\bar{n} = 4$. The logical error probabilities for both the surface codes and the repetition codes are obtained from Monte Carlo simulations of $d_Z$ code cycles and one final round of perfect stabilizer measurement. We use the same minimum-weight-perfect-matching (MWPM) decoder as described in Ref. [58].

rates to the desired level. To compare the SC with the standard cat, we follow the literature and consider the concatenation with a repetition code[30] and a thin rotated surface code[58]. The surface-cat scheme can arbitrarily suppress the errors in a resource-efficient manner once the ratio between the loss rate $\kappa_1$ and the engineered dissipation rate $\kappa_2$ is below a certain threshold. The repetition-cat, on the other hand, cannot arbitrarily suppress the errors for a cat with constrained $\bar{n}$. Below a $\kappa_1/\kappa_2$ threshold, as the repetition code size increases, the logical $Z$ error rate is exponentially suppressed while the logical $X$ error is linearly amplified. Thus, a minimal total logical error rate is present.

The concatenated schemes with the cat face several challenges. First, the $\kappa_1/\kappa_2$ thresholds (e.g., $\sim 5 \times 10^{-4}$ for the surface-cat in Fig. 4a. See also a comparable estimation in ref. [58]) are very low because of the low-fidelity bias-preserving operations. Also, the minimal logical error probability of the repetition-cat (e.g., $\sim 10^{-2}$ for $\bar{n} = 4$, see Fig. 4d) is not low enough for fault-tolerant algorithms, except for cats with very large mean photon number, because of the limited noise bias.

In the following, we will show that these challenges can be overcome by using the dissipative SC. The $\kappa_1/\kappa_2$ thresholds for both the surface code and the repetition code can be significantly improved by concatenating with the dissipative SC. Moreover, the repetition-SC can reach sufficiently low logical error probability $\sim 10^{-15}$ even with a small SC $\bar{n} = 4$ (see Fig. 4d). It is worth noticing that the thresholds for concatenated cat code shown in Fig. 4a, c are approximately independent of the size of the cat since the optimal CNOT gate error is independent of $\bar{n}$ for cat code.

We first consider the concatenation of the SC with a $d_X$ by $d_Z$ thin surface code. Similar to ref. [58], we fix the X distance $d_X$ to 3, which suffices to suppress the logical $X$ error rate, and increase the $Z$ distance $d_Z$ to suppress the logical $Z$ error rate. At fixed $\eta = 1/4$, we obtain the logical $Z$ error probability for $d_Z$ code cycles as a function of $\kappa_1/\kappa_2$ for different $d_Z$, as shown in Fig. 4a. The physical error rates of each physical operation involved in the surface-code QEC are presented in Supplementary Note 5. We obtain a $\kappa_1/\kappa_2$ threshold at 0.93%, which is around 20 times higher than that of the surface-cat[58]. Note that by optimizing the choice of the squeezing, the maximum threshold we obtained for $\bar{n} = 4$ is around 1.2%. Moreover, in Fig. 4b we show that this threshold can be further increased to about 3% by increasing $\bar{n}$ to 7. Note that the $\kappa_1/\kappa_2$ threshold of the surface-cat remains almost the same when increasing $\bar{n}$. We attribute the increase of the $\kappa_1/\kappa_2$ threshold (for the concatenated SC schemes) to the reduced physical-operation error rates (see the previous section).

Next we consider the concatenation of the SC with a repetition code with size $d_Z$. As shown in Fig. 4c, we obtain a 3.9%$\kappa_1/\kappa_2$ threshold for the logical $Z$ error rate (again, see Supplementary Note 5 for the physical error rates used for the simulation), which is roughly nine times higher than that of the repetition-cat. Below the $\kappa_1/\kappa_2$ threshold, as previously mentioned, a minimal total logical error rate is present. To obtain the minimal total logical error rate (by optimizing over $d_Z$), we find approximate expressions for the logical $Z$ and $X$ error probabilities in the sub-threshold regime ($\kappa_1/\kappa_2 < 10^{-3}$):

$$p_L^Z \approx 0.059 d_Z \left(\frac{p_Z'}{0.056}\right)^{0.48 d_Z}, \qquad p_L^X \approx 2 d_Z (d_Z - 1) p_{X,Y}, \tag{14}$$

where $p_Z' := p_{Z_t} + p_{Z_c Z_t}$ denotes the sum of the target-mode and the correlated phase-flip rate of the CNOT gate (phase flips on the control mode have negligible contribution to the logical error rate for the repetition code), $p_{X,Y}$ the total non-$Z$ error rates of the CNOT gate (the total rates of all the two-qubit Pauli errors that do not contain $Z$ terms). $p_Z'$ and $p_{X,Y}$ are in general functions of the CNOT gate time $\kappa_2 T$. To obtain simple expressions for them, we restrict the CNOT gate time to be $\kappa_2 T \geq 1$, which limits the nonadiabatic leakage during the gate. In this regime, we have $p_Z' \approx \kappa_1 \bar{n} T$, $p_{X,Y} \approx 5.57 \times \frac{e^{-2\alpha'^2}}{\alpha'^2} \frac{1}{\kappa_2 T}$. Note that we do not see the contribution from the loss rate $\kappa_1$ to $p_{X,Y}$ since for fast gate, $p_{X,Y}$ is dominated by the nonadiabatic errors.

In Fig. 4d, we plot the minimal total logical error probability $p_L = p_L^Z + p_L^X$ of the repetition-SC by optimizing $d_Z$ and $\kappa_2 T$ for $\bar{n} = 4$ and $\eta = 1/4$. As a comparison, we also include minimal logical error probabilities of the repetition-cat with $\bar{n} = 4$ using the physical error rates in ref. [58]. When $\kappa_1/\kappa_2 \geq 10^{-3}$, the optimal

gate error is no longer attained under the long gate time constraint, $\kappa_2 T \geq 1$ for the SC. Therefore, in that regime, the SC results can be understood as an upper bound of the minimum total logical error rates. For a practical noise ratio $\kappa_1/\kappa_2 = 10^{-3}$, the minimal logical error probability of the repetition-SC can reach $\sim 10^{-15}$, which suffices for many useful quantum computational tasks[8,51]. In contrast, the logical error probability of the repetition-cat (with $\overline{n} = 4$) can only reach $\sim 10^{-2}$, which is far from being useful. Even with a larger cat size of $\overline{n} = 8$ as considered in, e.g., ref. [58], the minimum logical error probability is still roughly $\sim 10^{-5}$ at such a noise ratio. To reach a similar level of logical error probability as the repetition-SC, we need either a much larger cat with $\overline{n} \gg 10$ (with the repetition code), or a more sophisticated outer code, e.g., the surface code. We attribute the drastic reduction in the minimal logical error rate of the repetition-SC to the significantly enhanced noise bias, or equivalently, the reduced physical bit-flip rates of the SC, which are exponentially suppressed by $\overline{n}^2$, instead of $\overline{n}$ for the cat.

## DISCUSSION

Although in this work we benchmark the performance of the concatenated codes as a function of $\kappa_1/\kappa_2$ for both the cat and the SC, it might be of different difficulty level to engineer the same dissipation rate $\kappa_2$ for the cat and the SC, depending on the hardware implementation. Therefore, we can compare the performance of the concatenated codes as a function of $\kappa_1/M$, where $M$ is the physical rate that is most challenging to engineer in practice. Here we focus on the implementation in superconducting circuits.

For example, a potential hardware challenge is to engineer strong nonlinear couplings. In this case, we can compare the concatenated codes as a function of $\kappa_1/J_m$, where $J_m$ denotes the largest nonlinear coupling strength required. For the cat, $J_m$ is simply given by $g_2$, the strength of the two-photon exchange Hamiltonian $g_2\left(\hat{a}^2\hat{b}^\dagger + h.c.\right)$. Assuming an adiabaticity constraint $\epsilon$, the lossy mode can be adiabatically eliminated, and $J_m = \sqrt{\overline{n}}\kappa_2/2\epsilon$[42,58]. For the SC, as shown in the Methods, the maximum nonlinear coupling strength is given by $J_m = \alpha' \sinh 2r\kappa_2/\sqrt{\epsilon_0}$. Here, $\epsilon_0$ is the relevant adiabatic condition for our proposed stabilization scheme using three bosonic modes.

Using these relations, we can change the horizontal axis in Fig. 4a to $\kappa_1/J_m$ and obtain about a 3.5 times increase in the $\kappa_1/J_m$ threshold for the surface-SC compared to the surface-cat. Furthermore, results in Fig. 4a are obtained by optimizing the parameters, such as the squeezing $r$ and the gate times, with the target function set to be the threshold in $\kappa_1/\kappa_2$. If the target function is set to the threshold in $\kappa_1/J_m$ instead, it is likely that the optimal code parameters are different, and the corresponding threshold could be further increased. Based on these considerations, we expect that the SC should maintain advantages over the cat even considering the experimental constraints (which will be hardware-specific) in the circuit level. We leave it to future work on optimizing the hardware design and quantifying the hardware-specific improvement.

To better understand the novelty and necessity of the partity-flipping dissipator $\hat{F}$ we introduced in Eq. (7), we compare it with a parity-preserving dissipator

$$\hat{F}' = \hat{S}(r)(\hat{a}^2 - \alpha'^2)\hat{S}^\dagger(r) \approx 2\alpha'\hat{I}_L \otimes \hat{\tilde{a}}, \tag{15}$$

which is a straightforward extension from $\hat{a}^2 - \alpha^2$ that stabilizes the cat. Such a dissipator was recently considered in ref. [71] for stabilizing the SC. We show that the extra phase-flip correction in $\hat{F}$ is essential for reducing SC's error rate in both the memory level and gate operations, which then leads to better logical performance in the concatenated level.

**Table 1.** Comparison of the optimal gate error rates for the SC and the cat. All errors are normalized by the optimal gate errors of the cat, which are given by $p_{Z(\theta)} = \frac{\theta}{2}\sqrt{\frac{1}{\overline{n}}\frac{\kappa_1}{\kappa_2}}$ and $p_{\mathrm{CNOT}} = \frac{\pi}{2\sqrt{2}}\sqrt{\frac{\kappa_1}{\kappa_2}}$[58]. The definitions of $\hat{F}$ and $\hat{F}'$ are given in Eq. (7) and Eq. (15) respectively. The optimal gate errors for SC are reached at $\eta \approx \frac{1}{2}$. The optima $Z(\theta)$ gate time for SC with $\hat{F}'$ and $\hat{F}$ are approximately $\frac{\pi}{4\sqrt{\kappa_1\kappa_2}}\overline{n}^{-5/2}$ and $\frac{\pi}{4\sqrt{3\kappa_1\kappa_2}}\overline{n}^{-7/2}$ respectively. The gate times for CNOT are approximately $\frac{\pi}{4\sqrt{2\kappa_1\kappa_2}}\overline{n}^{-3/2}$ and $\frac{\pi}{12\sqrt{\kappa_1\kappa_2}}\overline{n}^{-5/2}$ respectively. Since the cooling time is mostly assumed to be constant in our gate scheme, it is neglected for simplicity. We only provide the scaling of the gate errors with $\overline{n}$ for the SC since the exact expressions are complicated, as shown in Methods.

| Normalized gate error | SC with $\hat{F}'$ | SC with $\hat{F}$ |
|---|---|---|
| $Z(\theta)$ | $1/(\overline{n}+1)$ | $\sim \overline{n}^{-2}$ |
| CNOT | $2/\sqrt{\overline{n}+1}$ | $\sim \overline{n}^{-3/2}$ |

In the memory level, the change of a parity flip on the dissipator does not affect the bit-flip error rate we derived in Eq. (11). So a SC stabilized by $\hat{F}'$ can also have a favorable scaling between the minimal bit-flip rate and $\overline{n}$: $\gamma_{X,Y} \propto e^{-2\overline{n}}$. Nevertheless, $\hat{F}'$ lacks the parity flip $Z_L$ that corrects the detectable portion of the loss-induced errors, as shown clearly from Fig. 1 (the missing of the blue arrow). Therefore, a SC stabilized by $\hat{F}'$ is not capable of correcting the loss errors. As such, it suffers from the same phase-flip error rate as a cat, $\gamma_Z = \kappa_1\overline{n}$.

Regarding the gate operations, we take the Z rotation and the CNOT gate as examples. For the Z rotation, a SC stabilized by $\hat{F}'$ only enjoys a suppression in the non-adiabatic errors by the the increased adiabatic gap, $4\kappa_2\alpha'^2$, compared to conventional cat of the same $\overline{n}$. In contrast, a SC stabilized by $\hat{F}$ corrects the leading-order non-adiabatic error in $1/\alpha'^2$, since the the extra $\hat{Z}_L$ in $\hat{F}$ compensates the parity-flip associated with the non-adiabatic transition (to the leading order). The residual errors are proportion to the correction factor, $\xi \propto 1/\alpha'^2$, as discussed in Methods (see Eq. (33)). Therefore, while the minimal $Z(\theta)$ gate error for the SC with $\hat{F}'$ is roughly suppressed by a factor $1/\overline{n}$ compared to the cat, that for the SC with $\hat{F}$ is suppressed by an $1/\overline{n}^2$ factor (see Table 1).

The errors of CNOT operation can be analyzed in a similar fashion. Due to the enlarged adiabatic gap, the minimal $Z$ error rate of our SC gate with $\hat{F}'$ is a factor of $\frac{2}{\sqrt{\overline{n}+1}}$ smaller than that of the cat gate[30]. For the mean excitation number we consider, $\overline{n} = 4$, this factor is only slightly less than 1. However, with the parity-flipping dissipator $\hat{F}$, the gate error enjoys a $\eta$ suppression in the loss errors and an additional $\propto 1/\alpha'^2$ suppression in the non-adiabatic error. Combining these advantages, the CNOT gate error ratio with that of the cat roughly scales as $\overline{n}^{-3/2}$ (see Table 1).

Since the fault-tolerant threshold is mostly limited by errors of the CNOT and the idling operation, the thresholds of the concatenated SC schemes using $\hat{F}'$ is comparable to that of the concatenated cat scheme even at optimal squeezing for small mean excitation number. As such, having the extra phase-flip correction in the dissipator $\hat{F}$ is crucial for concatenated QEC and fault-tolerant quantum computing.

The stabilized cat qubits have been considered as a candidate for hardware-efficient, fault-tolerant, and scalable computation tasks in superconducting circuits[58,68]. The dissipative SC, which we show has an overall advantage over the cat, could play an important role along this direction.

The dissipative SC could also find its application in trapped-ion systems. On the one hand, encoding into the motional states of the ions provides an alternative approach for storing and protecting the quantum information. How to process the

information (e.g., implementing quantum gates) remains to be explored. On the other hand, if the information is stored in the internal states of the ions (the conventional approach), the bosonic codes like the SC could lead to more robust information processing. One could utilize multi-species ions[72,73] with multiple levels[74] and dissipatively protect the motional modes while leaving a subset of the ions' internal states that carry the information intact. The protected motional modes can, for instance, be used for scalable, parallel, and high-quality entangling gates mediated by localized phonon modes[75].

## METHODS

### Physical realization of the dissipator

In this section, we present the details of the two approaches implementing the dissipator in Eq. (7). Before describing our recipes, it is worth discussing the challenges involved here. The most straightforward method to realizing a generic Lindblad dissipator $\mathcal{D}[\hat{F}]$ is to couple the system to an auxiliary reservoir mode $c$ (with decay rate $\kappa_c$) via a coupling Hamiltonian $g(\hat{F}\hat{c}^\dagger + h.c.)$. In the limit where mode $c$ acts as a Markovian environment for the system, i.e., $\kappa_c \gg g$, we realize the target dissipator $\hat{F}$ with an effective dissipation rate $4g^2/\kappa_c$. For the dissipator in Eq. (7), this simple route requires a strong fourth-order nonlinear coupling, which has not been demonstrated yet due to the experimental challenges.

Here we present two approaches for realizing the desired nonlinear dissipator using accessible experimental resources: The first approach utilizes three nonlinearly-coupled bosonic modes, which can be physically realized in, e.g., superconducting circuits[42,43]; The second approach couples a bosonic mode nonlinearly to a qutrit, which can be physically realized in, e.g., trapped-ion system[44].

The first approach only requires third-order nonlinearities, which can be experimentally generated by four-wave fixing, to implement our desired dissipator, making use of a more structured engineered dissipation proposed in ref. [62]. Under the subsystem decomposition of the storage mode $a$ encoding the SC, one can realize a general nonlinear dissipator of the form $\mathcal{D}[e^{-i\theta\hat{Z}_L} \otimes \hat{\tilde{A}}]$ (with an angle $\theta$), by coupling a gauge-mode operator $\hat{\tilde{A}}$ and an auxiliary mode $b$ to the input and output ports of a directional waveguide, respectively, and introducing a

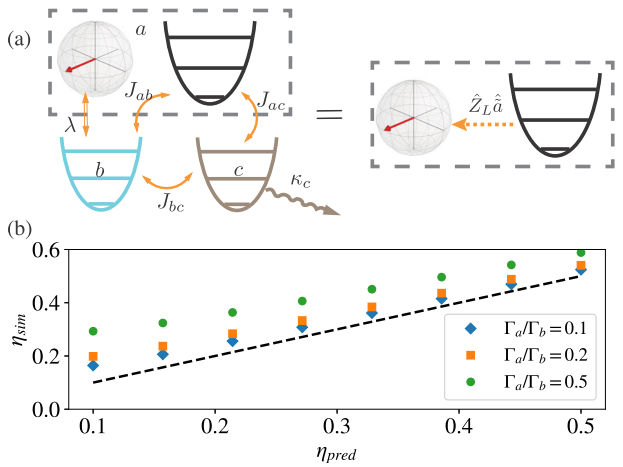


**Fig. 5 Physical realization of the stabilized SC in superconducting circuits. a** Realization of the parity-flipping dissipator $\hat{Z}_L \otimes \hat{\tilde{a}}$ using three nonlinearly coupled bosonic modes. **b** Comparison between the numerically extracted $\eta$ ($\eta_{\text{sim}}$) and the theoretically predicted $\eta$ ($\eta_{\text{pred}}$ in Eq. (6)) for a range of finite $\Gamma_a/\Gamma_b$. The dashed line indicates the ideal case where $\eta_{\text{sim}} = \eta_{\text{pred}}$.

dispersive interaction between an auxiliary mode $b$ and the logical qubit: $\hat{H}_{\text{disp.}} = \frac{\lambda}{2}\hat{Z}_L\hat{b}^\dagger\hat{b}$. For the dissipator in Eq. (7), we choose $\hat{\tilde{A}} = \hat{\tilde{a}}$. The physical interactions (in the Fock basis) can be obtained from the mapping $\hat{\tilde{a}} \to \frac{1}{2\alpha'}\hat{S}(r)(\hat{a}^2 - \alpha'^2)\hat{S}^\dagger(r)$, and $\hat{Z}_L \to \frac{1}{2\alpha'}\hat{S}(r)\left(\hat{a} + \hat{a}^\dagger\right)\hat{S}^\dagger(r)$, which means that we need a nonlinear coupling between the storage mode $a$ and the waveguide port. While it is challenging to directly achieve this using e.g., a physical circulator, the directional dynamics can be synthetically engineered by adding another reservoir mode $c$. The whole setup is illustrated in Fig. 5a, whose dynamics is given by master equation

$$\frac{d}{dt}\hat{\rho} = -i[\hat{H}_{\text{disp.}} + \hat{H}_{\text{tun.}}, \hat{\rho}] + \kappa_c\mathcal{D}[\hat{c}], \tag{16}$$

where the tunnel coupling Hamiltonian $\hat{H}_{\text{tun.}}$ of the total system-reservoir is given by

$$\hat{H}_{\text{tun.}} = J_{ab}\hat{\tilde{a}}^\dagger\hat{b} + (J_{ac}\hat{\tilde{a}} - iJ_{bc}\hat{b})\hat{c}^\dagger + h.c., \tag{17}$$

$$J_{ab} = \sqrt{\Gamma_a\Gamma_b}/2,\ J_{ac} = \sqrt{\Gamma_a\kappa_c}/2,\ J_{bc} = \sqrt{\Gamma_b\kappa_c}/2. \tag{18}$$

In the regime where the joint $b,c$ modes act as a Markovian reservoir for mode $a$, i.e., $\kappa_c \gg \sqrt{\Gamma_a\Gamma_b}$ and $\Gamma_b \gg \Gamma_a$, we can adiabatically eliminate both $b$ and $c$ to obtain an effective dissipator (using the effective operator formalism[76]), as

$$\frac{d}{dt}\hat{\rho} = \Gamma_a\mathcal{D}\left[\frac{i\lambda\hat{Z}_L - \Gamma_b}{i\lambda\hat{Z}_L + \Gamma_b}\hat{\tilde{a}}\right]\hat{\rho}. \tag{19}$$

Setting $\lambda = \Gamma_b$, we obtain the desired dissipator $\hat{Z}_L \otimes \hat{\tilde{a}}$ to stabilize the SC (see Supplementary Note 6 for a detailed derivation).

When deriving Eq. (19), we require the physical setup Eq. (16) to operate in the regime where adiabatic elimination remains valid. It is thus natural to ask what are the imperfections given realistic physical parameters, i.e., when the decay rates $\kappa_c$, $\Gamma_b$ of auxiliary modes $b,c$ cannot be infinitely large. In that case, one can show the dominating error due to finite reservoir bandwidth is due to the finite decay rates $\kappa_c$ and $\Gamma_b$, and it is preferable to set $\kappa_c \sim \Gamma_b$ to optimize over hardware resources (see Supplementary Note 6 for details). In this regime, the extra error introduced by physical implementation is determined by the ratio $\Gamma_a/\Gamma_b$, which heuristically describes the branching ratio between the logical qubit population that does not undergo the parity flip (uncorrected error) and the population that does (corrected error) whenever a gauge mode excitation decays into the environment. More specifically, as shown in Supplementary Note 6, we can approximately derive the discrepancy between the desired suppression factor for the loss-induced phase flip rate $\eta_{\text{pred}}$ (using Eq. (6)) and the numerically extracted (achievable) value $\eta_{\text{sim}}$, as $\eta_{\text{sim}} - \eta_{\text{pred}} = (1 - \eta_{\text{pred}})(\Gamma_a/2\Gamma_b)$. As shown in Fig. 5b, by setting $\Gamma_a/\Gamma_b = 0.1$, we can realize the desired $\eta$ within 50% accuracy.

To make the required nonlinearity more clear, we can also explicitly write down the physical Hamiltonian Eq. (16) in the Fock basis:

$$\begin{aligned}\hat{H}_{\text{tun.}} &= \tfrac{J}{2\alpha'}\hat{a}_s^{\dagger 2}(\hat{b} + \hat{c}) - \tfrac{J}{2}\alpha'(\hat{b} + \hat{c}) - \tfrac{i}{2}\kappa_c\hat{b}\hat{c}^\dagger + h.c.,\\ \hat{H}_{\text{disp.}} &= \tfrac{\kappa_c e^r}{4\alpha'}(\hat{a} + \hat{a}^\dagger)\hat{b}^\dagger\hat{b},\end{aligned} \tag{20}$$

where $\hat{a}_s = \cosh r\hat{a} + \sinh r\hat{a}^\dagger$ is the squeezed annihilation operator, and $J := \sqrt{\Gamma_a\kappa_c}/2$. We have assumed that $\kappa_c = \Gamma_b = \lambda$. $\hat{H}_{\text{tun.}}$ involves several cubic nonlinear couplings between the $a,b$ modes and between the $a,c$ modes. In addition, $\hat{H}_{\text{tun.}}$ requires a resonant linear coupling between the $b,c$ modes and some linear drives with strength $\frac{J\alpha'}{2}$ on the $b,c$ modes that pump energy into the system. Note that all the nonlinear terms are cubic, which have been experimentally demonstrated in superconducting circuits[42,43]. The maximum nonlinear coupling strength is

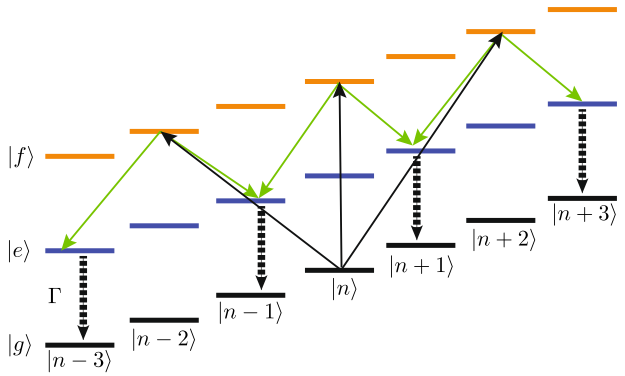


**Fig. 6 Laser configuration for the coupling Hamiltonian in Eq. (22) for implementing the SC in trapped-ion system.** The motional mode of the ion is coupled to three internal states via the sideband transitions, represented by the black and green arrows. Starting from $|g\rangle\otimes|\psi\rangle$ ($|\psi\rangle$ is an arbitrary motional state), the system goes through a two-step coherent transition $|g\rangle\otimes|\psi\rangle\to|f\rangle\otimes\hat{F}_1|\psi\rangle\to|e\rangle\otimes\hat{F}_2\hat{F}_1|\psi\rangle$ (indicated by the black and the green solid arrows, respectively) and decays rapidly to $|g\rangle\otimes\hat{F}_2\hat{F}_1|\psi\rangle$ (indicated by the black dashed arrows). Here $\hat{F}_1\propto\hat{S}(r)(\hat{a}^2-\alpha'^2)\hat{S}^\dagger(r)$ and $\hat{F}_2\propto\hat{S}(r)\hat{a}\hat{S}^\dagger(r)$. Adiabatically eliminating the $|e\rangle,|f\rangle$ states, we obtain the effective dissipator on the motional mode $\hat{F}=\hat{F}_2\hat{F}_1$.

$J_m:=J\sinh 2r/2\alpha'$. Now we can write $\kappa_2$ as a function of $J_m$ and $\kappa_c$. Comparing the dissipator $\sqrt{\Gamma_a}\hat{Z}_L\otimes\hat{a}$ in Eq. (19) with the dissipator $\sqrt{\kappa_2}\hat{F}\approx\sqrt{\kappa_2}2\alpha'\hat{Z}_L\otimes\hat{a}$, we have $\kappa_2=\Gamma_a/4\alpha'^2$, so that $\kappa_2=\frac{4J_m^2}{\kappa_c\sinh^2 2r}$. If we take $\Gamma_a=\epsilon_0\kappa_c$ (and correspondingly, $\kappa_c=\frac{4\alpha' J_m}{\sqrt{\epsilon_0}\sinh 2r}$), where $\epsilon_0<1$ is related to the adiabatic elimination condition discussed above, we can obtain $J_m=\alpha'\sinh 2r\kappa_2/\sqrt{\epsilon_0}$.

Now we present the second approach for implementing the dissipator $\hat{F}=\frac{1}{\alpha'}\hat{S}(r)\hat{a}(\hat{a}^2-\alpha'^2)\hat{S}^\dagger(r)$ using a coupled boson-qutrit system. Note that a simpler dissipator stabilizing a cat $\hat{a}^2-\alpha^2$ was obtained using a coupled boson-qubit system in trapped-ion platform in ref. [44]. However, the dissipator $\hat{F}$ cannot be directly engineered using their approach since there are many frequency-degenerate terms, e.g., $\hat{a}$ and $\hat{a}^\dagger\hat{a}^2$, that cannot be independently controlled by a single sideband drive. To resolve this, we generalize their approach by introducing a third internal level of the ion, and implementing the dissipator $\hat{F}$ in two steps associated with different electronic transitions. Specifically, we use the motional mode of the ions in a 1D harmonic trap as the bosonic mode, which is coupled to three internal levels $|g\rangle,|e\rangle$ and $|f\rangle$ via several laser beams:

$$\frac{d}{dt}\hat{\rho}=-i[\hat{H}_{\text{eff}},\hat{\rho}]+\mathcal{J}\hat{\rho}, \tag{21}$$

where $\hat{H}_{\text{eff}}=\nu\hat{a}^\dagger\hat{a}+\omega_e|e\rangle\langle e|+\omega_f|f\rangle\langle f|+\frac{1}{2}\Omega_0(|f\rangle\langle g|e^{-i\omega_f t}+h.c.)+\hat{H}_{\text{coup}}-i\frac{\Gamma}{2}|e\rangle\langle e|$, with

$$\begin{aligned}\hat{H}_{\text{coup}}=&\sum_{i=1}^{3}\Omega_i\cos[\eta_0(\hat{a}+\hat{a}^\dagger)](|f\rangle\langle g|e^{-i(\omega_f+\delta_i)t}+h.c.)\\&+\sum_{i=4}^{5}\Omega_i\sin[\eta_0(\hat{a}+\hat{a}^\dagger)](|e\rangle\langle f|e^{-i(\omega_e-\omega_f+\delta_i)t}+h.c.),\end{aligned} \tag{22}$$

and

$$\begin{aligned}J\hat{\rho}=&\Gamma\int_{-1}^{1}duN(u)e^{-i\eta_0 u\left(\hat{a}+\hat{a}^\dagger\right)}\\&\times|g\rangle\langle e|\hat{\rho}|e\rangle\langle g|e^{i\eta_0 u\left(\hat{a}+\hat{a}^\dagger\right)}.\end{aligned} \tag{23}$$

Here $\nu$ is the trap frequency, $\eta_0$ the Lamb-Dick parameter, $\Gamma$ the engineered decay rate from $|e\rangle$ to $|g\rangle$, and $N(u)$ the normalized dipole pattern. $\hat{H}_{\text{coup}}$ describes the coupling between the motional mode and the internal states, illustrated in Fig. 6, and $\mathcal{J}\hat{\rho}$ describes the spontaneous emission of the ion from $|e\rangle$ to $|g\rangle$ and its associated momentum kicks. The drive with amplitude $\Omega_0$ in $\hat{H}_{\text{eff}}$ comes from a laser that is coupled to the ion along a constrained (transverse) direction, thereby only driving the internal transitions. By tuning the laser detunings $\delta_1=-2\nu,\delta_2=2\nu,\delta_3=0,\delta_4=-\nu$, and $\delta_5=\nu$, and choosing appropriate driving strength $\{\Omega_i\}$ (see Supplementary Note 6), we can obtain a coupling Hamiltonian (neglecting the fast-rotating terms):

$$\begin{aligned}\hat{H}_{\text{coup}}=&\Omega'_{gf}\hat{S}(r)(\hat{a}^2-\alpha'^2)\hat{S}^\dagger(r)|f\rangle\langle g|\\&+\Omega'_{ef}\tfrac{1}{\alpha'}\hat{S}(r)\hat{a}\hat{S}^\dagger(r)|e\rangle\langle f|+h.c.\end{aligned} \tag{24}$$

In the regime where $2\alpha'\Omega'_{gf}\ll\Gamma$, $\Omega'_{gf}\ll\Omega'_{ef}$, we can obtain a reduced dynamics on the motional mode by adiabtically eliminating the $|e\rangle,|f\rangle$ states:

$$\frac{d}{dt}\hat{\rho}_m=\kappa_2\mathcal{D}[\hat{F}]\hat{\rho}_m, \tag{25}$$

where $\hat{\rho}_m$ is the reduced density matrix on the motional mode. Through numerically simulations we find that we can obtain the dissipator $\hat{F}$ with the desired rate by setting $\Omega'_{ef}=0.5\Gamma$, $\Omega'_{gf}/\Omega'_{ef}=1/20$. A large $\kappa_2$, therefore, demands large $\Gamma$ and driving strength. Note that we have assumed that $\Gamma$ and $\{\Omega_i\}, i=1,2,3,4,5$ are much smaller than $\nu$, so that the off-resonant terms can be safely neglected (secular approximation). In practice, however, one might be able to go beyond this weak-drive regime by carefully canceling the effects from the off-resonant terms. We have also neglected the effects from the momentum kicks here, which only lead to a small increase in the phase-flip suppression factor $\eta\to\eta+\mathcal{O}(\eta_0^2)$. See Supplementary Note 6 for a more detailed analysis. We stress that our proposed approach requires the same order of nonlinearity as that required by a two-component cat, which has been considered to be feasible in trapped-ion system[44].

### The memory error rates of the squeezed cat

In this section, we provide the derivation of the memory error rates for the SC in Eqs. (10) and (11).

Since the bit-flip error rate is exponentially small in $\alpha'$, the subsystem decomposition is insufficient to obtain an analytical expression of it. Thus, we derive the bit-flip error rate using the conserved quantities of the system[29,65]. To facilitate the analysis, we first neglect the $\hat{Z}_L$ term in the dissipator in Eq. (7) since it does not contribute to the bit-flip rate, and then analyze the system dynamics in the squeezed frame:

$$\frac{d\hat{\rho}_s}{dt}=\kappa_2\mathcal{D}[\hat{a}^2-\alpha'^2]\hat{\rho}_s+\kappa_\phi\mathcal{D}[\hat{a}_s^\dagger\hat{a}_s]\hat{\rho}_s, \tag{26}$$

where $\hat{A}_s:=\hat{S}^\dagger(r)\hat{A}\hat{S}(r)$ for any operator $\hat{A}$. Note that we we consider the dephasing here, which is the dominant source for the bit-flip errors. The two conserved quantities associated with the dominant dissipator $\hat{a}^2-\alpha'^2$ are

$$\begin{aligned}\hat{J}_{++}&=\sum_{n=0}^{\infty}|2n\rangle\langle 2n|,\\\hat{J}_{+-}&=\sqrt{\tfrac{2\alpha'^2}{\sinh 2\alpha'^2}}\sum_{q=-\infty}^{\infty}\tfrac{(-1)^q}{2q+1}I_q(\alpha'^2)\hat{J}_{+-}^{(q)},\end{aligned} \tag{27}$$

where $I_q(\cdot)$ is the modified Bessel function of the first kind, and $\hat{J}_{+-}^{(q)}=\frac{(\hat{a}^\dagger\hat{a}-1)!!}{(\hat{a}^\dagger\hat{a}+2q)!!}\hat{J}_{++}\hat{a}^{2q+1}$ for $q\geq 0$ and $\hat{J}_{+-}^{(q)}=\hat{J}_{++}\hat{a}^{\dagger 2q+1}\frac{(\hat{a}^\dagger\hat{a})!!}{(\hat{a}^\dagger\hat{a}+2|q|-1)!!}$ for $q<0$. The steady state coherence of the system initialized in $\hat{\rho}(0)$ can be computed through $c_{++}(\infty)=\text{tr}\left\{J_{++}^\dagger\rho(0)\right\}$ and $c_{+-}(\infty)=\text{tr}\left\{J_{+-}^\dagger\rho(0)\right\}$. Thus, we compute the bir-flip rate perturbatively by considering the dephasing in the squeezed

frame,

$$\gamma_{X,Y} = -\kappa_\phi \,\mathrm{tr}\left\{J_{+-}^{\dagger}\mathcal{D}\left[\hat{S}^{\dagger}(r)\hat{a}^{\dagger}\hat{a}\hat{S}(r)\right]|C_\alpha^+\rangle\langle C_\alpha^-|\right\}, \tag{28}$$

which is then simplified to Eq. (11).

The phase-flip error rate Eq. (10) can be easily derived by analyzing the errors under the subsystem decomposition. The loss and heating errors are in the form $\hat{a} \approx \hat{Z}_L \otimes (e^{-r}\alpha' + \cosh r\hat{\tilde{a}} - \sinh r\hat{\tilde{a}}^{\dagger})$, $\hat{a}^{\dagger} \approx \hat{Z}_L \otimes (e^{-r}\alpha' + \cosh r\hat{\tilde{a}}^{\dagger} - \sinh r\hat{\tilde{a}})$. They both contribute to the phase-flip rate via the undetectable term $e^{-r}\alpha'\hat{Z}_L = \sqrt{\eta\bar{n}}\hat{Z}_L$ (the detectable part associated with the $\hat{Z}_L \otimes \hat{\tilde{a}}^{\dagger}$ term is approximately correctable by $\hat{F}$). The dephasing is in the form $\hat{a}^{\dagger}\hat{a} \approx \hat{I}_L \otimes [e^{-2r}\alpha'^2 + e^{-2r}\alpha'(\hat{\tilde{a}} + \hat{\tilde{a}}^{\dagger}) + \cosh^2 r\hat{\tilde{a}}^{\dagger}\hat{\tilde{a}} + \sinh^2 r\hat{\tilde{a}}\hat{\tilde{a}}^{\dagger} - \cosh r \sinh r(\hat{\tilde{a}}^2 + \hat{\tilde{a}}^{\dagger 2})]$. It contributes to the phase-flip rate dominantly by the $e^{-2r}\alpha'\hat{I}_L \otimes \hat{\tilde{a}}^{\dagger}$ term, which creates an excitation in the gauge mode that is subsequently destroyed by $\hat{F}$ with a residual phase flip. Therefore, the dephasing contributes to the phase-flip rate by $\kappa_\phi e^{-4r}\alpha'^2 = \kappa_\phi e^{-2r}\eta\bar{n}$.

Eq. (10) is valid in the regime where $\alpha' \gg 1$, which is violated when $r$ approaches the maximum squeezing allowed by the energy constraint. We now provide a leading-order correction to the loss-induced phase flip rate in such a regime. We have assumed that the dissipator $\hat{F} = \hat{Z}_L(\hat{a}^2 - \alpha^2) \approx \hat{Z}_L \otimes (\hat{\tilde{a}}^2 + 2\alpha'\hat{\tilde{a}})$ can perfectly correct the detectable part of the loss-(or heating-) induced errors by removing the excitation in the gauge mode while applying a phase-flip correction on the logical qubit. However, it is not a perfect correction because of the non-Hermitian part of the dynamics induced by $F^{\dagger}F \approx \hat{I}_L \otimes [\hat{\tilde{a}}^{\dagger 2}\hat{\tilde{a}}^2 + 2\alpha'(\hat{\tilde{a}}^{\dagger 2}\hat{\tilde{a}} + \hat{\tilde{a}}^{\dagger}\hat{\tilde{a}}^2) + 4\alpha'^2\hat{\tilde{a}}^{\dagger}\hat{\tilde{a}}]$. The second term above further excites the gauge mode, which introduces additional non-negligible Z errors when $\alpha' \gg 1$ does not hold. Through analysis of a simplified 3-level system, we obtain a correction factor for the phase-flip rate in the form of

$$\xi = \frac{1}{2(1+3\alpha'^2)}, \tag{29}$$

which works well for $\alpha' \geq 1.5$. This factor represents that, if the qubit evolves from an initial state of $|\pm\rangle_L \otimes |\bar{n}=1\rangle$ under the dissipator $\hat{F}$, a population of $1-\xi$ would end up in $|\mp\rangle_L \otimes |\bar{n}=0\rangle$ and $\xi$ would be in $|\pm\rangle_L \otimes |\bar{n}=0\rangle$ in steady state. Therefore, the phase-flip rate in Eq. (10) has an extra correction:

$$\gamma_Z \to \gamma_Z + \kappa_1(1+n_{\mathrm{th}})\bar{n}(1-\eta)\xi + \kappa_1 n_{\mathrm{th}}(1-\eta')\xi - \kappa_\phi e^{-2r}\eta\xi, \tag{30}$$

where $\eta' = (\bar{n} - \cosh^2 r)/\bar{n}$, which approaches $\eta$ in the large squeezing limit.

The correction factor's effect becomes significant as $\eta$ approaches 0. In the limit of large $\bar{n}$ and only considering the dominant loss error, the Z error rate has a minimum value $\gamma_{Z,\min} \approx \frac{\sqrt{2}}{4}\kappa_1$. Worth noticing, this minimum rate is independent of $\bar{n}$. Therefore, the SC enjoys an exponential suppression of the bit-flip rate while maintaining a bounded phase-flip rate by increasing $\bar{n}$, which is drastically different from the cat code or its DV counterpart, the repetition code.

### Bias-preserving operations for the squeezed cat

In this section, we present the detailed design and error analysis for the $Z$ rotation $Z(\theta)$ and the CNOT gate for the SC, which are representatives of bias-preserving opearations $\mathcal{B}$. See Supplementary Note 4 for the rest of the operations in $\mathcal{B}$.

Similarly to the cat, the $Z$-axis rotation $Z(\theta)$ can be generated by a resonant linear drive

$$\hat{H}_Z = \frac{\theta}{4\alpha' T}e^{r}(\hat{a} + \hat{a}^{\dagger}), \tag{31}$$

in the presence of the engineered dissipation in Eq. (7) for a time $T$. In the subsystem basis, $H_Z \approx \frac{\theta}{4\alpha' T}\hat{Z}_L \otimes (2\alpha' + \hat{\tilde{a}} + \hat{\tilde{a}}^{\dagger})$. The total phase flip error probability of the $Z$ rotation is $p_Z = p_Z^{\mathrm{NA}}(T) + \kappa_1\eta\bar{n}T$, where the second term represents the loss-induced phase flips and the first term represents the non-adiabatic errors due to the non-adiabatic excitation $\hat{Z}_L \otimes \hat{\tilde{a}}^{\dagger}$ in $\hat{H}_Z$. We note that compared to the parity-preserving dissipator $\mathcal{D}[\hat{I}_L \otimes \hat{\tilde{a}}]$, which is used in the literature for the cat (by applying a driven two-photon dissipation), the parity-flipping dissipator $\hat{F}$ in Eq. (7) can significantly reduce the non-adiabatic errors induced by $\hat{Z}_L \otimes \hat{\tilde{a}}^{\dagger}$. The reason is that the majority of the parity flips associated with the non-adiabatic transitions can be flipped back through the application of the dissipator. The remaining errors with a fraction $\xi$ leads to the residual non-adiabatic error $p_Z^{\mathrm{NA}}$ proportional to $\xi$ (see the previous Methods section). Under the adiabatic limit $\frac{\theta}{4\alpha' T} \ll 4\kappa_2\alpha'^2$, the system's evolution under the dissipator $\hat{F}$ can be approximated by the dynamics of the density matrix $\hat{\rho}_{\mathrm{trunc}}$ with a truncated 2-level gauge basis:

$$\kappa_2\mathcal{D}[\hat{F}]\hat{\rho} \approx 4\kappa_2\alpha'^2((1-\xi)\mathcal{D}[\hat{Z}_L \otimes \hat{\tilde{a}}] + \xi\mathcal{D}[\hat{I}_L \otimes \hat{\tilde{a}}])\hat{\rho}_{\mathrm{trunc}}. \tag{32}$$

Performing first-order adiabatic elimination[76] on the gauge excited state results in an effective Z error rate $\frac{\xi\theta^2}{16\kappa_2\alpha'^4 T^2}$. Notice that adiabatic elimination does not capture the higher-order errors and the result only holds under the adiabatic limit. A more accurate expression can be derived through solving the ordinary differential equations of the two level system. As a result, the modified non-adiabatic error has the form:

$$p_Z^{\mathrm{NA}}(T) = \frac{\xi\theta^2}{16\kappa_2\alpha'^4 T^2}\left(c_1 T + c_2\frac{e^{-2\kappa_2\alpha'^2 T} - 1}{2\kappa_2\alpha'^2}\right). \tag{33}$$

Performing numerical fit, we obtain $c_1 = 1.5, c_2 = 1.8$.

The CNOT gate is implemented by applying the engineered dissipation only on the control mode and a Hamiltonian term that drives a phase rotation on the target mode conditioned on the states of the control mode:

$$\begin{aligned} &\tfrac{d}{dt}\hat{\rho} = \kappa_2\mathcal{D}[\hat{F}_c]\hat{\rho} - i[\hat{H}_{\mathrm{CNOT}}, \hat{\rho}], \\ &\hat{H}_{\mathrm{CNOT}} = \tfrac{\pi}{4\alpha' T}\left[e^{r}(\hat{a}_c + \hat{a}_c^{\dagger}) - 2\alpha'\right](\hat{a}_t^{\dagger}\hat{a}_t - \alpha'^2), \end{aligned} \tag{34}$$

where $\hat{F}_c$ denotes the engineered dissipator in Eq. (7) on the control mode. The noise terms are not shown for simplicity. We note that compared to the standard CNOT gate on the cat[30,58], we turn off the dissipation on the target mode during the gate to circumvent the need for high-order coupling terms between the two modes. Although the target mode temporarily loses the protection against the excitation loss, we can still implement a high-quality gate if the gate time is short enough and the leakage on the target mode can be subsequently returned to the code space without introducing too many errors. Similar strategy and insights have been made in ref. [77]. To deal with the non-adiabatic transitions on the target mode, which preserve the parity, we apply a parity-preserving dissipation $\kappa_2\mathcal{D}[\hat{S}(r)(\hat{a}_t^2 - \alpha'^2)\hat{S}^{\dagger}(r)]$ on the target mode (while the control mode is, as always, protected by the parity-flipping dissipation) for a time $T_{\mathrm{cool}}$. In our simulations, we fix the cooling time $T_{\mathrm{cool}} = 8\times\frac{1}{4\kappa_2\alpha'^2}$ to ensure that the leakage is suppressed to below 0.5%. Using the Pauli-twirling approximation, the Z-type errors of the CNOT gate are

$$\begin{aligned} &p_{Z_c} = \kappa_1\eta\bar{n}(T + T_{\mathrm{cool}}) + p_Z^{\mathrm{NA}}(T), \\ &p_{Z_t} = \kappa_1\bar{n}\left(\tfrac{T}{2} + T_{\mathrm{cool}}\right), \\ &p_{Z_cZ_t} = \tfrac{1}{2}\kappa_1\bar{n}T, \end{aligned} \tag{35}$$

where $p_{Z_c}, p_{Z_t}$ and $p_{Z_cZ_t}$ denote the $Z$ error on the control, target mode and the correlated $Z$ error, respectively. They sum to the total Z error probability $p_Z = \kappa_1\bar{n}(1+\eta)(T+T_{\text{cool}}) + p_Z^{\text{NA}}(T)$. Note that, unlike the $Z$ rotation, the CNOT gate does not enjoy a full suppression of the loss-induced errors (by a factor $\eta$) due to the lack of the engineered dissipation on the target mode during the gate. The non-adiabatic error $p_Z^{\text{NA}}(T)$ on the control mode has a similar form as Eq. (33):

$$p_Z^{\text{NA}}(T) = \frac{\xi\pi^2}{16\kappa_2\alpha'^2T^2}\left(1.5T + 0.6\frac{e^{-2\kappa_2\alpha'^2T}-1}{2\kappa_2\alpha'^2}\right) \tag{36}$$

We also present the non-$Z$ error rate of the CNOT gate here. Note that the CNOT gate has a significantly larger non-$Z$ error rate than all other bias-preserving operations in $\mathcal{B}$. As discussed numerically in ref. [58], the non-$Z$ error of a cat's CNOT gate scales approximately as $1.8\frac{e^{-2\alpha^2}}{\alpha^2}\frac{1}{\kappa_2 T}$. For our CNOT gate on the SC, we find a similar expression

$$p_{X,Y} = 5.57\frac{e^{-2\alpha'^2}}{\alpha'^2}\frac{1}{\kappa_2 T}, \tag{37}$$

in the regime where $\kappa_2 T > 1$. Note that for shorter gate time, we cannot find a simple expression for $p_{X,Y}$ and a numerical simulation of the gate has to be performed to determine $p_{X,Y}$.

## DATA AVAILABILITY

The Python codes and numerical simulation results are available from the corresponding author upon reasonable request.

Received: 30 November 2022; Accepted: 21 July 2023;
Published online: 03 August 2023

## REFERENCES

1. Nielsen, M. A. & Chuang, I. L. *Quantum computation and quantum information: 10th anniversary* Edition (Cambridge University Press, Cambridge, United Kingdom, 2010).
2. Lidar, D. A. & Brun, T. A. *Quantum error correction* (Cambridge University Press, Cambridge, United Kingdom, 2013).
3. Aharonov, D., Ben-Or, M., Impagliazzo, R. & Nisan, N. Limitations of noisy reversible computation. Preprint at https://arxiv.org/abs/quant-ph/9611028 (1996).
4. Aharonov, D. & Ben-Or, M. Fault-tolerant quantum computation with constant error. In *Proc. Annual. ACM Symposium*., 176–188 (1997).
5. Kitaev, A. Y. Quantum computations: algorithms and error correction. *Russ. Math. Surv.* **52**, 1191 (1997).
6. Knill, E., Laflamme, R. & Zurek, W. H. Resilient quantum computation: error models and thresholds. *Proc. R. Soc. A: Math. Phys. Eng. Sci.* **454**, 365–384 (1998).
7. Aliferis, P., Gottesman, D. & Preskill, J. Quantum accuracy threshold for concatenated distance-3 codes. *Quantum Info. Comput.* **6**, 97–165 (2006).
8. Fowler, A. G., Mariantoni, M., Martinis, J. M. & Cleland, A. N. Surface codes: towards practical large-scale quantum computation. *Phys. Rev. A* **86**, 032324 (2012).
9. Litinski, D. A game of surface codes: large-scale quantum computing with lattice surgery. *Quantum* **3**, 128 (2019).
10. Chao, R., Beverland, M. E., Delfosse, N. & Haah, J. Optimization of the surface code design for majorana-based qubits. *Quantum* **4**, 352 (2020).
11. Beverland, M. E., Kubica, A. & Svore, K. M. Cost of universality: a comparative study of the overhead of state distillation and code switching with color codes. *PRX Quantum* **2**, 020341 (2021).
12. Gottesman, D., Kitaev, A. & Preskill, J. Encoding a qubit in an oscillator. *Phys. Rev. A* **64**, 012310 (2001).
13. Chuang, I. L., Leung, D. W. & Yamamoto, Y. Bosonic quantum codes for amplitude damping. *Phys. Rev. A* **56**, 1114 (1997).
14. Michael, M. H. et al. New class of quantum error-correcting codes for a bosonic mode. *Phys. Rev. X* **6**, 031006 (2016).
15. Cochrane, P. T., Milburn, G. J. & Munro, W. J. Macroscopically distinct quantum-superposition states as a bosonic code for amplitude damping. *Phys. Rev. A* **59**, 2631 (1999).
16. Albert, V. V. et al. Performance and structure of single-mode bosonic codes. *Phys. Rev. A* **97**, 032346 (2018).
17. Ofek, N. et al. Extending the lifetime of a quantum bit with error correction in superconducting circuits. *Nature* **536**, 441–445 (2016).
18. Hu, L. et al. Quantum error correction and universal gate set operation on a binomial bosonic logical qubit. *Nat. Phys.* **15**, 503–508 (2019).
19. Campagne-Ibarcq, P. et al. Quantum error correction of a qubit encoded in grid states of an oscillator. *Nature* **584**, 368–372 (2020).
20. Lescanne, R. et al. Exponential suppression of bit-flips in a qubit encoded in an oscillator. *Nat. Phys.* **16**, 509–513 (2020).
21. Flühmann, C. et al. Encoding a qubit in a trapped-ion mechanical oscillator. *Nature* **566**, 513–517 (2019).
22. Grimm, A. et al. Stabilization and operation of a kerr-cat qubit. *Nature* **584**, 205–209 (2020).
23. Egan, L. et al. Fault-tolerant control of an error-corrected qubit. *Nature* **598**, 281–286 (2021).
24. Zhao, Y. et al. Realization of an error-correcting surface code with superconducting qubits. *Phys. Rev. Lett.* **129**, 030501 (2022).
25. Ryan-Anderson, C. et al. Implementing fault-tolerant entangling gates on the five-qubit code and the color code. Preprint at https://arxiv.org/abs/2208.01863 (2022).
26. Acharya, R. et al. Suppressing quantum errors by scaling a surface code logical qubit. *Nature* **614**, 676–681 (2023).
27. Lebreuilly, J., Noh, K., Wang, C.-H., Girvin, S. M. & Jiang, L. Autonomous quantum error correction and quantum computation. Preprint at https://arxiv.org/abs/2103.05007 (2021).
28. Lihm, J.-M., Noh, K. & Fischer, U. R. Implementation-independent sufficient condition of the knill-laflamme type for the autonomous protection of logical qudits by strong engineered dissipation. *Phys. Rev. A* **98**, 012317 (2018).
29. Mirrahimi, M. et al. Dynamically protected cat-qubits: a new paradigm for universal quantum computation. *New. J. Phys.* **16**, 045014 (2014).
30. Guillaud, J. & Mirrahimi, M. Repetition cat qubits for fault-tolerant quantum computation. *Phys. Rev. X* **9**, 041053 (2019).
31. Puri, S., Boutin, S. & Blais, A. Engineering the quantum states of light in a kerr-nonlinear resonator by two-photon driving. *Npj Quantum Inf.* **3**, 18 (2017).
32. Putterman, H. et al. Stabilizing a bosonic qubit using colored dissipation. *Phys. Rev. Lett.* **128**, 110502 (2022).
33. Berdou, C. et al. One hundred second bit-flip time in a two-photon dissipative oscillator. *PRX Quantum* **4**, 020350 (2023).
34. Kwon, S., Watabe, S. & Tsai, J.-S. Autonomous quantum error correction in a four-photon kerr parametric oscillator. *Npj Quantum Inf.* **8**, 40 (2022).
35. Grimsmo, A. L., Combes, J. & Baragiola, B. Q. Quantum computing with rotation-symmetric bosonic codes. *Phys. Rev. X* **10**, 011058 (2020).
36. Royer, B., Singh, S. & Girvin, S. Stabilization of finite-energy gottesman-kitaev-preskill states. *Phys. Rev. Lett.* **125**, 260509 (2020).
37. Gertler, J. M. et al. Protecting a bosonic qubit with autonomous quantum error correction. *Nature* **590**, 243–248 (2021).
38. Schlegel, D. S., Minganti, F. & Savona, V. Quantum error correction using squeezed schrödinger cat states. *Phys. Rev. A* **106**, 022431 (2022).
39. Reimpell, M. & Werner, R. F. Iterative optimization of quantum error correcting codes. *Phys. Rev. Lett.* **94**, 080501 (2005).
40. Fletcher, A. S., Shor, P. W. & Win, M. Z. Optimum quantum error recovery using semidefinite programming. *Phys. Rev. A* **75**, 012338 (2007).
41. Noh, K., Albert, V. V. & Jiang, L. Quantum capacity bounds of gaussian thermal loss channels and achievable rates with gottesman-kitaev-preskill codes. *IEEE Trans. Inf.* **65**, 2563–2582 (2018).
42. Leghtas, Z. et al. Confining the state of light to a quantum manifold by engineered two-photon loss. *Science* **347**, 853–857 (2015).
43. Touzard, S. et al. Gated conditional displacement readout of superconducting qubits. *Phys. Rev. Lett.* **122**, 080502 (2019).
44. Poyatos, J., Cirac, J. I. & Zoller, P. Quantum reservoir engineering with laser cooled trapped ions. *Phys. Rev. Lett.* **77**, 4728 (1996).
45. Tuckett, D. K., Bartlett, S. D. & Flammia, S. T. Ultrahigh error threshold for surface codes with biased noise. *Phys. Rev. Lett.* **120**, 050505 (2018).
46. Tuckett, D. K. et al. Tailoring surface codes for highly biased noise. *Phys. Rev. X* **9**, 041031 (2019).
47. Tuckett, D. K., Bartlett, S. D., Flammia, S. T. & Brown, B. J. Fault-tolerant thresholds for the surface code in excess of 5% under biased noise. *Phys. Rev. Lett.* **124**, 130501 (2020).
48. Bonilla Ataides, J. P., Tuckett, D. K., Bartlett, S. D., Flammia, S. T. & Brown, B. J. The XZZX surface code. *Nat. Commun.* **12**, 1–12 (2021).
49. Roffe, J., Cohen, L. Z., Quintavalle, A. O., Chandra, D. & Campbell, E. T. Bias-tailored quantum LDPC codes. *Quantum* **7**, 1005 (2023).
50. Xu, Q. et al. Tailored xzzx codes for biased noise. *Phys. Rev. Res.* **5**, 013035 (2023).

51. O'Gorman, J. & Campbell, E. T. Quantum computation with realistic magic-state factories. *Phys. Rev. A* **95**, 032338 (2017).
52. Teh, R., Drummond, P. & Reid, M. Overcoming decoherence of schrödinger cat states formed in a cavity using squeezed-state inputs. *Phys. Rev. Res.* **2**, 043387 (2020).
53. Lo, H.-Y. et al. Spin–motion entanglement and state diagnosis with squeezed oscillator wavepackets. *Nature* **521**, 336–339 (2015).
54. Le Jeannic, H., Cavaillès, A., Huang, K., Filip, R. & Laurat, J. Slowing quantum decoherence by squeezing in phase space. *Phys. Rev. Lett.* **120**, 073603 (2018).
55. Lau, H.-K. & Clerk, A. A. High-fidelity bosonic quantum state transfer using imperfect transducers and interference. *Npj Quantum Inf.* **5**, 31 (2019).
56. Pan, X. et al. Protecting the quantum interference of cat states by phase-space compression. *Phys. Rev. X* **13**, 021004 (2023).
57. Pantaleoni, G., Baragiola, B. Q. & Menicucci, N. C. Modular bosonic subsystem codes. *Phys. Rev. Lett.* **125**, 040501 (2020).
58. Chamberland, C. et al. Building a fault-tolerant quantum computer using concatenated cat codes. *PRX Quantum* **3**, 010329 (2022).
59. Bennett, C. H., DiVincenzo, D. P., Smolin, J. A. & Wootters, W. K. Mixed-state entanglement and quantum error correction. *Phys. Rev. A* **54**, 3824 (1996).
60. Knill, E. & Laflamme, R. Theory of quantum error-correcting codes. *Phys. Rev. A* **55**, 900 (1997).
61. Gross, J. A., Caves, C. M., Milburn, G. J. & Combes, J. Qubit models of weak continuous measurements: Markovian conditional and open-system dynamics. *Quantum Sci. Technol.* **3**, 024005 (2018).
62. Wang, Y.-X., Wang, C. & Clerk, A. A. Quantum nonreciprocal interactions via dissipative gauge symmetry. *PRX Quantum* **4**, 010306 (2023).
63. Puri, S. et al. Bias-preserving gates with stabilized cat qubits. *Sci. Adv.* **6**, eaay5901 (2020).
64. Guillaud, J. & Mirrahimi, M. Error rates and resource overheads of repetition cat qubits. *Phys. Rev. A* **103**, 042413 (2021).
65. Albert, V. V. Lindbladians with multiple steady states: theory and applications. Preprint at https://arxiv.org/abs/1802.00010 (2018).
66. Leviant, P., Xu, Q., Jiang, L. & Rosenblum, S. Quantum capacity and codes for the bosonic loss-dephasing channel. *Quantum* **6**, 821 (2022).
67. Bonilla Ataides, J. P., Tuckett, D. K., Bartlett, S. D., Flammia, S. T. & Brown, B. J. The XZZX surface code. *Nat. Commun.* **12**, 1–12 (2021).
68. Darmawan, A. S., Brown, B. J., Grimsmo, A. L., Tuckett, D. K. & Puri, S. Practical quantum error correction with the xzzx code and kerr-cat qubits. *PRX Quantum* **2**, 030345 (2021).
69. Xu, Q., Iverson, J. K., Brandão, F. G. & Jiang, L. Engineering fast bias-preserving gates on stabilized cat qubits. *Phys. Rev. Res.* **4**, 013082 (2022).
70. Yuan, M., Xu, Q. & Jiang, L. Construction of bias-preserving operations for pair-cat codes. *Phys. Rev. A* **106**, 062422 (2022).
71. Hillmann, T. & Quijandría, F. Quantum error correction with dissipatively stabilized squeezed-cat qubits. *Phys. Rev. A* **107**, 032423 (2023).
72. Inlek, I. V., Crocker, C., Lichtman, M., Sosnova, K. & Monroe, C. Multispecies trapped-ion node for quantum networking. *Phys. Rev. Lett.* **118**, 250502 (2017).
73. Bruzewicz, C. D., McConnell, R., Stuart, J., Sage, J. M. & Chiaverini, J. Dual-species, multi-qubit logic primitives for ca+/sr+ trapped-ion crystals. *Npj Quantum Inf.* **5**, 102 (2019).
74. Ringbauer, M. et al. A universal qudit quantum processor with trapped ions. *Nat. Phys.* **18**, 1053–1057 (2022).
75. Olsacher, T. et al. Scalable and parallel tweezer gates for quantum computing with long ion strings. *PRX Quantum* **1**, 020316 (2020).
76. Reiter, F. & Sørensen, A. S. Effective operator formalism for open quantum systems. *Phys. Rev. A* **85**, 032111 (2012).
77. Gautier, R., Sarlette, A. & Mirrahimi, M. Combined dissipative and hamiltonian confinement of cat qubits. *PRX Quantum* **3**, 020339 (2022).

## ACKNOWLEDGEMENTS

We thank Pei Zeng, Ramesh Bhandari, Yvonne Gao, Kyungjoo Noh for helpful discussions. We acknowledge support from the ARO (W911NF-18-1-0020, W911NF-18-1-0212, W911NF-19-1-0380), ARO MURI (W911NF-16-1-0349, W911NF-21-1-0325), AFOSR MURI (FA9550-19-1-0399, FA9550-21-1-0209), AFRL (FA8649-21-P-0781), DoE Q-NEXT, NSF (PHY-1748958, OMA-1936118, ERC-1941583, OMA-2137642), NTT Research, and the Packard Foundation (2020-71479).

## AUTHOR CONTRIBUTIONS

Q.X. conceived the project. Q.X., G.Z., and L.J. designed the AutoQEC protocol and fault-tolerant schemes using the SC qubit. Y.-X.W., A.A.C., and P.Z. provided expertize on physical realization of the AutoQEC protocol. Q.X. and G.Z. contributed to the work equally. Everyone contributed to writing the manuscript.

## COMPETING INTERESTS

The authors declare no competing interests.

## ADDITIONAL INFORMATION

**Supplementary information** The online version contains supplementary material available at https://doi.org/10.1038/s41534-023-00746-0.

**Correspondence** and requests for materials should be addressed to Liang Jiang.

**Reprints and permission information** is available at http://www.nature.com/reprints

**Publisher's note** Springer Nature remains neutral with regard to jurisdictional claims in published maps and institutional affiliations.